

Dispersion and mixing in heterogeneous compressible porous media under transient forcing

Satoshi Tajima¹, Marco Dentz²

¹Graduate School of Frontier Sciences, The University of Tokyo, Kashiwa, Japan

²Spanish National Research Council (IDAEA-CSIC), Barcelona, Spain

Abstract

Periodic forcing of flow in compressible porous media is an important driver for solute dispersion and mixing in geological and engineered porous media subject for example to tides, pumping and recharge cycles, or fluid injection and withdrawal cycles with a wide range of environmental and industrial applications. The combination of periodic forcing, spatial medium heterogeneity and medium compressibility leads to intricate spatio-temporal flow, dispersion and mixing patterns. We analyze these patterns using detailed numerical simulations based on a stochastic representation of the spatial medium heterogeneity. Solute dispersion is characterized by the interface length and width, mixing in terms of the dilution index and the distribution of concentration point values. Poincaré maps show how the interplay of heterogeneity and compressibility leads to the creation of stable regions that inhibit the advancement and dispersion of the mixing interface, and chaotic regions that at the same time enhance solute mixing. This means that spatial heterogeneity in combination with temporal forcing can lead to the containment of solute and at the same time promote mixing.

1 Introduction

Transient forcing of flow drives solute mixing and dispersion in compressible media through the interplay of temporal fluctuations, medium compressibility, and spatial heterogeneity. It plays a key role in mixing processes in geological and engineered porous media in response to tidal fluctuations, due to fluid injection and withdrawal cycles, and periodic pumping and recharge with broad environmental and engineering applications. For example, the salinity distribution in coastal aquifers controlled by transient forcing including tidal fluctuations (Oberdorfer et al., 1990; Inouchi et al., 1990; Pool et al., 2014; Ataie-Ashtiani et al., 1999) and infrequent events such as storm surges (Terry & Falkland, 2010; Bailey & Jenson, 2014; Tajima et al., 2023). In the context of underground hydrogen storage, hydrogen purity is determined by the mixing with the reservoir fluid (Zivar et al., 2021), which is enhanced by injection-production cycles.

Porous media have two primary characteristics that influence transient transport dynamics. First, porous media inherently exhibit heterogeneity across spatial scales. At the Darcy scale, such a heterogeneous structure is represented by heterogeneous hydraulic conductivity fields (Dagan, 2012; Dentz et al., 2023). Second, porous media are often compressible, which is quantified by a finite specific storage. This parameter denotes the volume of water released per unit decline in the hydraulic head, accompanied by a decrease in pore water pressure and an increase in effective stress. Finite storage attenuates the amplitude of periodic flow propagating into porous media and delays its phase (Jacob, 1950; Jiao & Tang, 1999; L. Li et al., 2000; H. Li & Jiao, 2002; Nielsen, 1990).

For incompressible porous media, perturbation analyses and numerical simulations have uncovered that velocity fluctuations in the mean flow direction minimally affect longitudinal dispersion parallel to the mean flow within heterogeneous porous media, whilst

Corresponding author: Satoshi Tajima, tajima@envsys.k.u-tokyo.ac.jp

exerting notable influence on transverse dispersion in the orthogonal direction (Kinzelbach & Ackerer, 1986; Rehfeldt & Gelhar, 1992; Dagan et al., 1996; Dentz & Carrera, 2003; Cirpka & Attinger, 2003; de Dreuzy et al., 2012). In highly heterogeneous porous media, temporal fluctuations in velocity reduce longitudinal spreading compared with steady-state conditions (de Dreuzy et al., 2012).

Pool et al. (2016) study the effects of finite storage on the evolution of displacement fronts under transient forcing in homogenous porous media using laboratory experiments, numerical simulations, and derive explicit analytical expression for the time-average transport dynamics. The combined effects of spatial heterogeneity and finite storage on dispersion were investigated by Pool et al. (2015), focusing on seawater intrusion under tidal fluctuations. Their numerical simulations reveal that increasing heterogeneity mitigates the spreading of the solute interface induced by periodic flow, while increased storage augments spreading. Pool and Dentz (2018) study the combined effect of medium compressibility, heterogeneity and variable density on reactive mixing patterns under temporal flow fluctuations. Their numerical simulations provide evidence that interface deformation due to spatial heterogeneity and temporal flow fluctuations together with density variation leads to the formation of complex patterns of reaction hotspots. It is still not clear, however, how medium heterogeneity and compressibility together with temporal flow fluctuations control the occurrence of Lagrangian coherent structures, and how they affect the advancement, dispersion and mixing dynamics of a solute interface aligned with the fluctuating pressure boundary. Recently, Wu et al. (2024) shed light on how Lagrangian coherent structures control solute dispersion in heterogeneous poroelastic media. To this end, these authors analyze the dispersion of point-like initial plumes under temporal fluctuations in the presence of a mean flow toward the fluctuating pressure boundary. They use a diffusive particle mapping method as a surrogate for the solution of the full advective-diffusive transport problem.

In this paper, we focus on the dispersion and mixing of a solute front that invades the medium from the fluctuating pressure boundary motivated by saltwater fronts in tidal aquifers, groundwater remediation measures through the period injection of reactants, and geostorage operations such as underground hydrogen storage. To this end, we first consider purely advective transport to elucidate the interplay between flow patterns and fluid deformation. Poincaré maps of the kinematic equations of motion of fluid particles in the flow field highlight the creation of stable (stagnant) and chaotic regions and their impact on large-scale solute dispersion. Detailed random walk particle tracking simulations quantify the impact of local-scale dispersion on the evolution of mixing fronts in terms of effective and ensemble dispersion coefficients, the mixing volume as measured by the dilution index, and the evolution of the probability density function of concentration point values. Our analysis sheds light on the intricate relation between flow and mixing patterns under transient forcing.

2 Basics and Methods

2.1 Flow

We consider transient flow and solute transport within a two-dimensional, fully saturated, confined, heterogeneous porous medium (Figure 1). Fluid mass and momentum balance are expressed by (Bear, 1988)

$$S_s \frac{\partial h(\mathbf{x}, t)}{\partial t} + \nabla \cdot \mathbf{q}(\mathbf{x}, t) = 0, \quad \mathbf{q}(\mathbf{x}, t) = -K(\mathbf{x}) \nabla h(\mathbf{x}, t), \quad (1)$$

where S_s is the specific storage, t is the time, $h(\mathbf{x}, t)$ is the hydraulic head, $\mathbf{q}(\mathbf{x}, t)$ is the Darcy flux, and $K(\mathbf{x})$ is the heterogeneous hydraulic conductivity. The heterogene-

ity of $K(\mathbf{x})$, assumed scalar for simplicity, is modelled as a multi-Gaussian spatial random field. The log-hydraulic conductivity $f(\mathbf{x}) = \ln K(\mathbf{x})$ is represented as a correlated Gaussian random space function with a mean $\bar{f} = \text{constant}$ and the exponential covariance function

$$\mathcal{C}_f(\mathbf{x}) = \sigma_f^2 \exp(-|\mathbf{x}|/\lambda) \quad (2)$$

where σ_f^2 is the variance of $f(\mathbf{x})$, λ its correlation length. The effective hydraulic conductivity is equal to the geometric mean conductivity $K_G = \exp(\bar{f})$ (Renard & de Marsily, 1997).

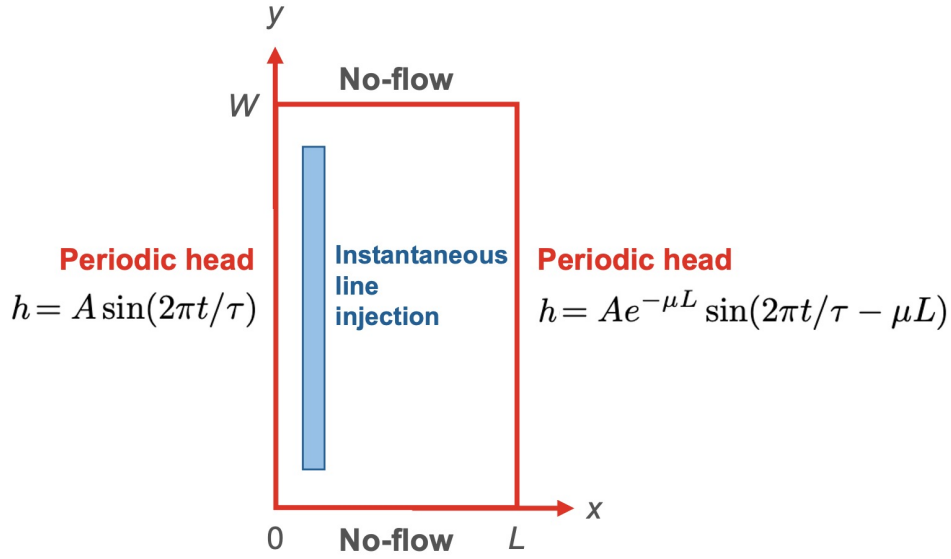


Figure 1. Schematic of model domain and boundary conditions.

We consider sinusoidal head fluctuations at $x = 0$ with amplitude A and period τ ,

$$h(\mathbf{x}, t)|_{x=0} = A \sin(2\pi t/\tau). \quad (3)$$

For a semi-infinite equivalent homogeneous medium with $K(\mathbf{x}) = K_G$, the analytical solution of Eq (1) is (Jacob, 1950; Ferris, 1952)

$$h_e(x, t) = A \exp(-\mu x) \sin(2\pi t/\tau - \mu x). \quad (4)$$

The wave number μ is defined as

$$\mu \equiv \sqrt{\frac{S_s \pi}{K_G \tau}}. \quad (5)$$

Its inverse gives the characteristic penetration distance of the periodic head fluctuation, or in other words, the head fluctuation decays exponentially fast on the length scale $1/\mu$. The corresponding Darcy flux is given by

$$q_e(x, t) = q_0 \exp(-\mu x) \sin\left(\frac{2\pi t}{\tau} - \mu x + \frac{\pi}{4}\right), \quad (6)$$

with the maximum flux

$$q_0 = \sqrt{2}AK_G\mu. \quad (7)$$

Figure 2 shows that the analytical solution (6) is an excellent descriptor of the vertically averaged streamwise flow velocity.

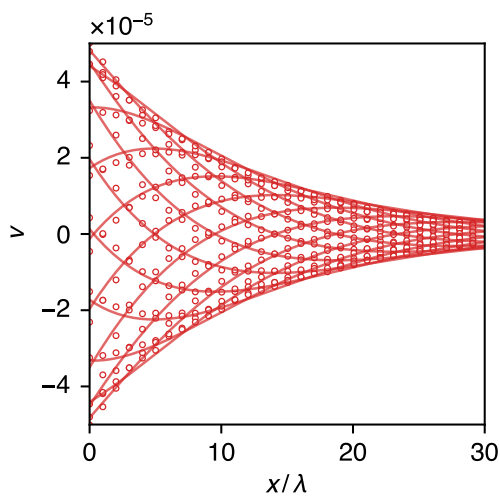


Figure 2. The symbols show the vertically averaged velocity $\bar{v}(x)$ at various times within one period for a heterogeneous medium with $\sigma_f^2 = 2.0$. The lines show the analytical solution for an equivalent homogeneous medium characterized by K_G .

Here we consider a finite two-dimensional medium of width W and length L . At the horizontal domain boundaries, we specify no-flow boundary conditions. At the right domain boundary at $x = L$, we set $h(x = L, t) = h_e(x = L, t)$ to emulate flow in a semi-infinite medium. Equation (1) is solved using MODFLOW 6 (Langevin et al., 2017). The simulation parameters are given in Table 1. The domain length is at least $8/\mu$, that is, 8 times the penetration depth. Steady-state conditions are achieved after a simulation time of $t = 100\tau$. Note that in the numerical transport simulations solute is injected when the flow field is in a steady state, which sets the time $t = 0$ for transport.

2.2 Transport

Transport is described by the advection-dispersion equation (Bear, 1988)

$$\frac{\partial c(\mathbf{x}, t)}{\partial t} = -\nabla \cdot \mathbf{u}(\mathbf{x}, t)c(\mathbf{x}, t) + \nabla \cdot [\mathbf{D}(\mathbf{x}, t)\nabla c(\mathbf{x}, t)], \quad (8)$$

where $c(\mathbf{x}, t)$ is the mass concentration, $\mathbf{u}(\mathbf{x}, t) = \mathbf{q}(\mathbf{x})/\phi$ is the pore water velocity. Here, we assume that porosity variability with pressure is small and set it equal to

Table 1. Parameters for numerical flow and transport simulations.

Parameter	Symbol	Value	Unit
Domain length	L	50λ	m
Domain width	W	30λ	m
Correlation length	λ	1	m
Geometric mean hydraulic conductivity	K_G	1×10^{-4}	m s^{-1}
Log-conductivity variance	σ_f^2	0, 0.25, 0.5, 1.0, 1.5, 1.75, 2.0	-
Amplitude	A	1	m
Period	τ	43200	s
Porosity	ϕ	0.25	-
Specific storage	S_s	1×10^{-2}	-
Initial line length	ℓ_0	0.8 W	m
Injection point	x_0	0.1 L	m
Dispersivity	α	$1 \times 10^{-3}, 5 \times 10^{-3}$	m
Péclet number	Pe	200, 1000	-

constant in the transport equation. Furthermore, the density of water is assumed to be constant, that is, it does not depend on the solute concentration. The local hydrodynamic dispersion tensor $\mathbf{D}(\mathbf{x}, t)$ is defined by (Bear, 1988)

$$D_{ij}(\mathbf{x}, t) = D_0\delta_{ij} + \delta_{ij}\alpha_I|\mathbf{u}(\mathbf{x}, t)| + (\alpha_I - \alpha_{II})\frac{u_i(\mathbf{x}, t)u_j(\mathbf{x}, t)}{|\mathbf{u}(\mathbf{x}, t)|}. \quad (9)$$

For simplicity, we assume that $D_0 = 0$ and $\alpha_I = \alpha_{II} \equiv \alpha$. Thus, $D_{ij} = \delta_{ij}\alpha|\mathbf{u}(\mathbf{x}, t)|$. The relative strength of advective and dispersive transport mechanisms is measured by the Péclet number

$$Pe \equiv \frac{\lambda}{\alpha}. \quad (10)$$

For $Pe \gg 1$, advection dominates. We consider an instantaneous injection along a line of length ℓ_0 at $x = x_0$ at time $t = 0$,

$$c(\mathbf{x}, t = 0) = \frac{1}{\ell_0}\delta(x - x_0), \quad (11)$$

where $\delta(x)$ denotes the Dirac delta. At the left and right domain boundaries, we specify absorbing boundary conditions. Note that no mass exits the domain during the simulation time, and thus the solute concentration integrates into one at any time.

The advection-dispersion equation (8) is equivalent to the Langevin equation (Kinzelbach, 1988; LaBolle et al., 2000),

$$\frac{d\mathbf{x}(t)}{dt} = \mathbf{u}[\mathbf{x}(t)] + \nabla \cdot \mathbf{D}[\mathbf{x}(t)] + \mathbf{B}[\mathbf{x}(t)] \cdot \boldsymbol{\zeta}(t), \quad (12)$$

where $\mathbf{B} \cdot \mathbf{B} = 2\mathbf{D}$, and $\boldsymbol{\zeta}(t)$ is a Gaussian white noise with zero mean and correlation function

$$\langle \zeta_i(t) \zeta_j(t') \rangle = \delta_{ij} \delta(t - t'). \quad (13)$$

The angular brackets denote the average over all noise realizations. We use here the Ito interpretation of the stochastic integral (Risken, 1996). The transport problem is solved numerically based on the Langevin equation (12) as outlined in detail in Appendix A. The concentration distribution $c(\mathbf{x}, t)$ is given in terms of the particle positions $\mathbf{x}(t)$ as

$$c(\mathbf{x}, t) = \langle \delta[\mathbf{x} - \mathbf{x}(t)] \rangle, \quad (14)$$

where $\delta(\mathbf{x})$ denotes the Dirac delta distribution. To reconstruct the concentration values from the particle positions, we use kernel density estimators (Fernández-García & Sánchez-Vila, 2011) as detailed in Appendix A.

Note that the velocity decreases exponentially with distance from the inlet on the length scale $\ell_c = 1/\mu$, the average penetration depth of the boundary pressure fluctuations. Thus, the interface starts decelerating when it reaches the distance ℓ_c . The characteristic time for deceleration is given by (Pool et al., 2016)

$$\tau_v = \frac{2\pi \exp(2\mu x_i)}{u_0^2 \mu^2 \tau}. \quad (15)$$

If $\ell_c < \lambda$, the mixing front starts decelerating before it can sweep over a correlation length of the medium. In other words, it experiences the medium heterogeneity as a quasi-stratified medium. The scenarios under consideration here are characterized by $\ell_c > 5\lambda$. Thus, the mixing interface can sweep more than one correlation length during a period τ . The transport parameters used in the numerical simulations are detailed in Table 1.

2.3 Observables

In the following, we define the observables used to characterize the dispersion and mixing behaviours. Dispersion is quantified in terms of the displacement statistics, specifically in terms of the displacement mean and variance, and the line length under purely advective transport. Mixing is quantified in terms of the statistics of the concentration point values, which are used to determine the mixing volume in terms of the dilution index, and the probability density function of concentration point values. All observables $\omega(t)$ are time averaged over one period τ of the periodic pressure fluctuation,

$$\bar{\omega}(t) \equiv \frac{1}{\tau} \int_0^\tau dt' \omega(t + t'). \quad (16)$$

The time average is denoted by an overbar. The observables defined in the following are compared to the corresponding analytical solutions for equivalent homogeneous media given in (Pool et al., 2016). For the convenience of the reader, these solutions are summarized in Appendix B.

2.3.1 Displacement statistics

To study the dispersion behaviour of the displacement front, we quantify the displacement mean and variance. To this end, we define the n -th displacement moment in a streamwise direction as

$$m_n(t) = \langle [x(t) - x_0]^n \rangle, \quad (17)$$

where the angle brackets denote the average over all the particles and medium realizations. The displacement mean and variance are defined in terms of the first and second displacement moments as

$$Z(t) = \overline{m_1}(t) \quad (18)$$

$$\sigma^2(t) = \overline{m_2}(t) - [\overline{m_1}(t)]^2. \quad (19)$$

The ensemble variance measures the spread of the mixing interface or the area swept by it. Furthermore, for purely advective transport, we consider the length of the displacement front, which is defined by

$$\ell(t) = \sum_i \sqrt{\Delta x_i(t)^2 + \Delta y_i(t)^2}, \quad (20)$$

where $\Delta x_i(t) = x_i(t, \mathbf{a} + \Delta \mathbf{a}) - x_i(t, \mathbf{a})$ and $\Delta y_i(t)$ accordingly. The sum runs over all line segments. For a homogeneous medium, $\ell(t) = \ell_0$ remains constant. Furthermore, we consider the dispersion of particle pairs initially separated by a small distance $|\Delta \mathbf{a}|$. Streamwise pair dispersion is quantified by

$$\sigma_{\text{eff}}^2(t) = \frac{1}{2} \overline{[x(t|\mathbf{a}) - x(t|\mathbf{a} + \Delta \mathbf{a})]^2}. \quad (21)$$

The effective variance is a measure of the width of the mixing interface (Kitanidis, 1988; Dentz et al., 2023).

2.3.2 Concentration statistics

To quantify the volume occupied by the solute, we use the dilution index (Kitanidis, 1994), which is defined by

$$E(t) = \overline{\exp[H(t)]}, \quad H(t) = - \int_{\Omega} d\mathbf{x} c(\mathbf{x}, t) \ln[c(\mathbf{x}, t)]. \quad (22)$$

The probability density function (PDF) of concentration point values is defined by

$$\Pi(c, t) = \frac{1}{V} \int_{\Omega} d\mathbf{r} \delta[c - c(\mathbf{x} + \mathbf{r}, t)], \quad (23)$$

where V is the volume of the domain Ω .

The concentration distribution for transport in an equivalent homogeneous medium can be approximated by the Gaussian concentration distribution (Pool et al., 2016)

$$c_0(\mathbf{x}, t) = \frac{1}{\ell_0} \frac{\exp\left[-\frac{[x - z_0(t)]^2}{2\sigma^2(t)}\right]}{\sqrt{2\pi\sigma^2(t)}}, \quad (24)$$

where the expressions for $z_0(t)$ and $\sigma_e^2(t)$ can be found in [Appendix B](#). The dilution index for this concentration distribution is given by

$$E_0(t) = \ell_0 \sqrt{2e\pi\sigma_e^2(t)}, \quad (25)$$

where e is the Euler constant. Based on this expression, we define a ‘‘mixing’’ variance $\sigma_{\text{mix}}^2(t)$ in terms of the dilution index $E(t)$ as

$$\sigma_{\text{mix}}^2(t) = \frac{1}{2e\pi} \left[\frac{E(t)}{\ell_0} \right]^2. \quad (26)$$

It describes the variance of a Gaussian distribution that occupies the same volume as the actual concentration distribution.

3 Results and discussion

We first consider purely advective transport to understand the stirring properties of the underlying flow field. To this end, we discuss the time evolution of the displacement mean and ensemble variance, and of the line length. Furthermore, we analyze Poincaré maps of the flow field, which give insight into the flow topology and its impact on the observed dispersion and mixing patterns. Second, we study dispersive transport and mixing to elucidate the interplay of temporal variability, medium compressibility and spatial heterogeneity on solute mixing. [Figure 3](#) shows the concentration distribution evolving from an initial lines source for homogeneous and heterogeneous media.

3.1 Purely advective transport and stirring

[Figure 4](#) shows the temporal evolution of the displacement mean, variance, and line length for different heterogeneity strengths σ_f^2 . [Figure 4a](#) shows that increasing σ_f^2 leads to a delay in the advance of the centre of mass $Z(t)$ compared to a homogeneous medium.

[Figures 4b](#) and [c](#) show that $\sigma^2(t)$ and $\ell(t)$ increase with time for heterogeneous media, while they are constant for equivalent homogeneous media. This is due to the heterogeneity-induced distortion of the line as shown in [Figure 3](#). With increasing $\sigma_f^2 < 1.5$, the ensemble variance, which measures the area swept by the line, increases as expected from macrodispersion theory for uniform flow (e.g. [Gelhar & Axness, 1983](#); [Dagan, 1982](#)).

However, for $\sigma_f^2 \geq 1.5$, a discernible reversal of trends is observed for times $\tau \gtrsim \tau_v$. Further increasing σ_f^2 leads to a slowing down of the temporal evolution of $\sigma^2(t)$ compared to the lower σ_f^2 cases. Thus, the effective area swept grows slower than for weak heterogeneity. The line length $\ell(t)$ in contrast increases steadily with increasing σ_f^2 . The line is stretched and deformed into a lamellar structure as shown in [Figure 3](#). At early times $t < \tau_v$, $\sigma(t)$ and $\ell(t)$ both are measures for the average interface length due to flow deformation. For large times, however, $\sigma(t)$ quantifies the extension of the area that is swept by the interface, that is, the support of the distorted line. The interface length increases by stretching and folding back on itself on a support whose growth rate decreases as illustrated in [Figure 3](#). That is, the increase of the tortuosity of the line by stretching and folding back on itself is stronger than the relative confinement due to the slowing down of the centre of mass position and ensemble variance.

In summary, increasing heterogeneity in porous media decelerates the advancement of the displacement front, that is, it leads to relative confinement of the particle plume and enhances line stretching and folding. These observations have implications for the

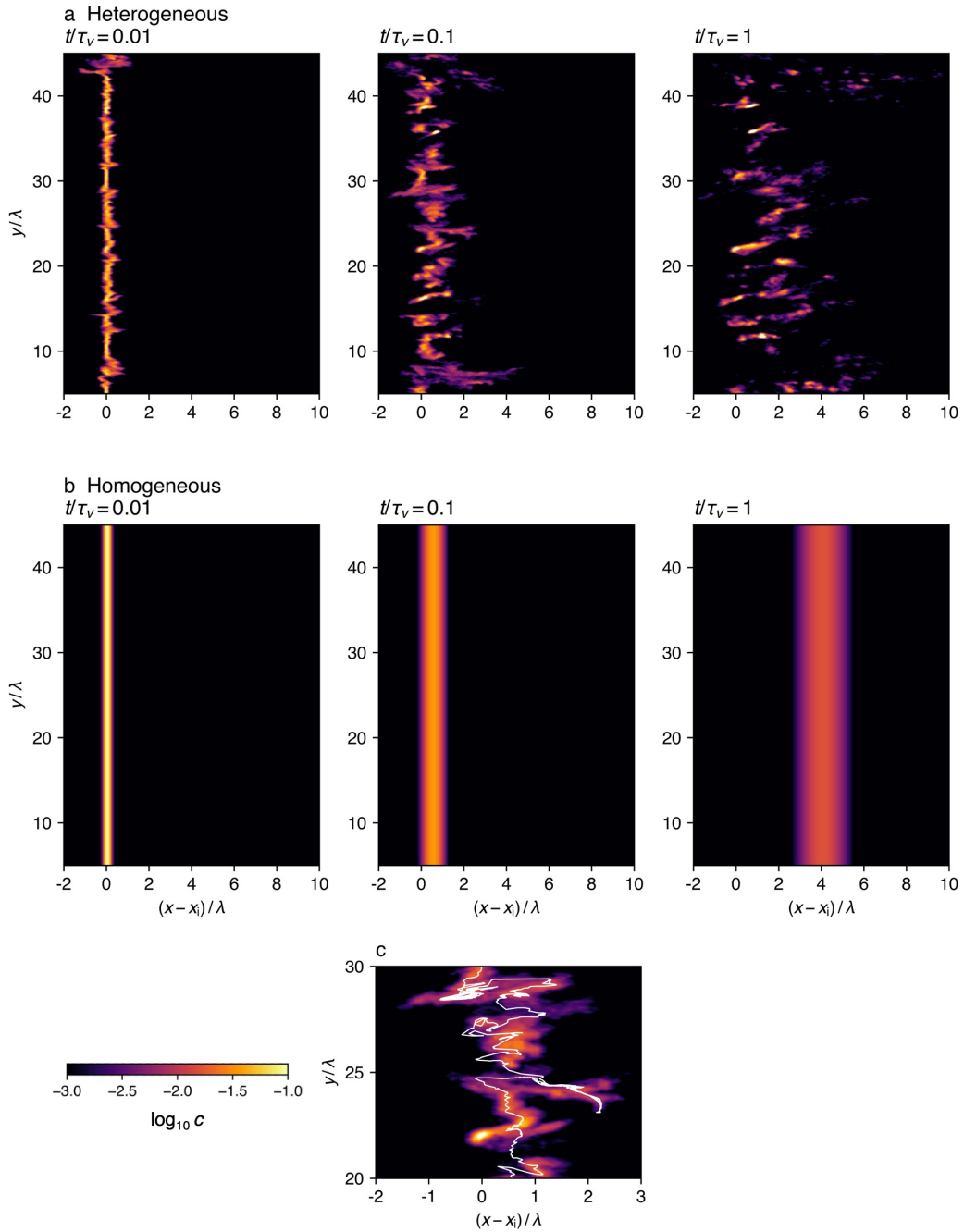


Figure 3. Temporal snapshots of concentration (c) distributions from (a) heterogeneous simulation results ($\sigma_f^2 = 2.0$) and (b) homogeneous analytical solutions (Equation B5) for $Pe = 1000$. (c) The concentration distribution for the heterogeneous medium with $\sigma_f^2 = 2.0$ at $t/\tau = 0.1$ is superposed by the purely advective line (shown by white).

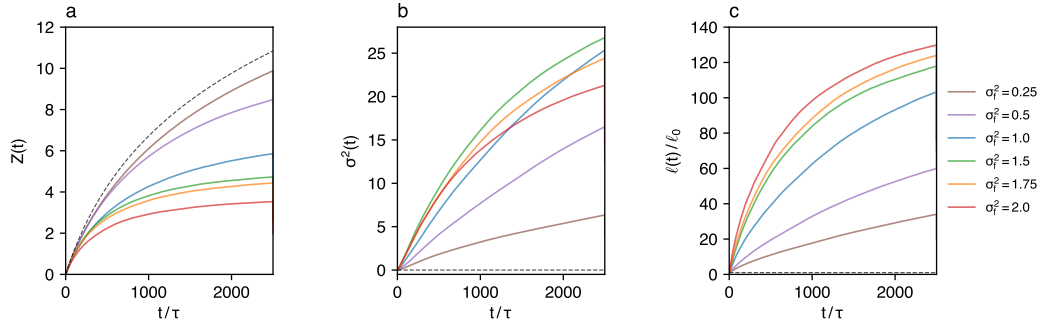


Figure 4. Temporal evolutions of period-averaged (a) centre of mass ($Z(t)$), (b) ensemble variance ($\sigma^2(t)$), and (c) displacement front length ($\ell(t)$) for various cases of $\ln K$ variance (σ_f^2). All cases are purely advective ($Pe = \infty$). Solid lines depict ensembled direct simulation results for heterogeneous media, and dashed lines are analytical expressions for homogeneous media ($\sigma_f^2 = 0$).

understanding of mixing in coastal aquifers, but also in the context of the design of groundwater remediation measures by reactant injection and mixing, as well as geological storage.

To understand these behaviours, we consider Poincaré maps of the underlying flow fields (Wu et al., 2024). Figure 5 shows snapshots of the positions of advectively transported particles at times $t/\tau = 1-1500$ for two different heterogeneity variances. Particles are initially seeded on a regular grid with spacing 0.2λ over the flow domain. The upper panels use the same colours for particles initialized in the same column, and the lower panels in the same row, to illustrate the quenching of particles originating from different horizontal or vertical positions in chaotic flow regions. We observe confined stable regions of particles that move on closed orbit, regular open trajectories, as well as chaotic regions. For $\sigma_f^2 = 2$, we observe less regular open trajectories and an increase in stable islands and chaotic regions compared to the case of weaker heterogeneity with $\sigma_f^2 = 0.5$. For an equivalent homogeneous medium, all trajectories are of course straight lines. The retention of particles in stable and confined chaotic regions explains the observations of Figure 4. The displacement mean slows down due to increased retention at increasing σ_f^2 . Similarly, the ensemble variance first increases with heterogeneity compared to a homogeneous media but then slows down again due to particle retention. The interface length on the other hand increases due to stretching and folding around the stable regions in subsequent flow periods.

3.2 Dispersive transport and mixing

In this section, we study solute dispersion and mixing in the presence of local scale dispersion, that is for finite local scale Pe . Figure 6a shows that the mean front displacement is larger for the high than for low Pe , while the mean displacement for the equivalent homogeneous medium is not affected by Pe . At large times, the displacements for finite Pe are both larger than for the purely advective case. This behaviour can be explained by the fact that finite dispersion can release particles from stable and confined regions, and promote transport in regular regions. Thus, the displacement mean first increases for finite Pe . However, when Pe is further increased, it decreases again because particles can be more efficiently been trapped in stagnant regions, which again leads to a retention of the plume.

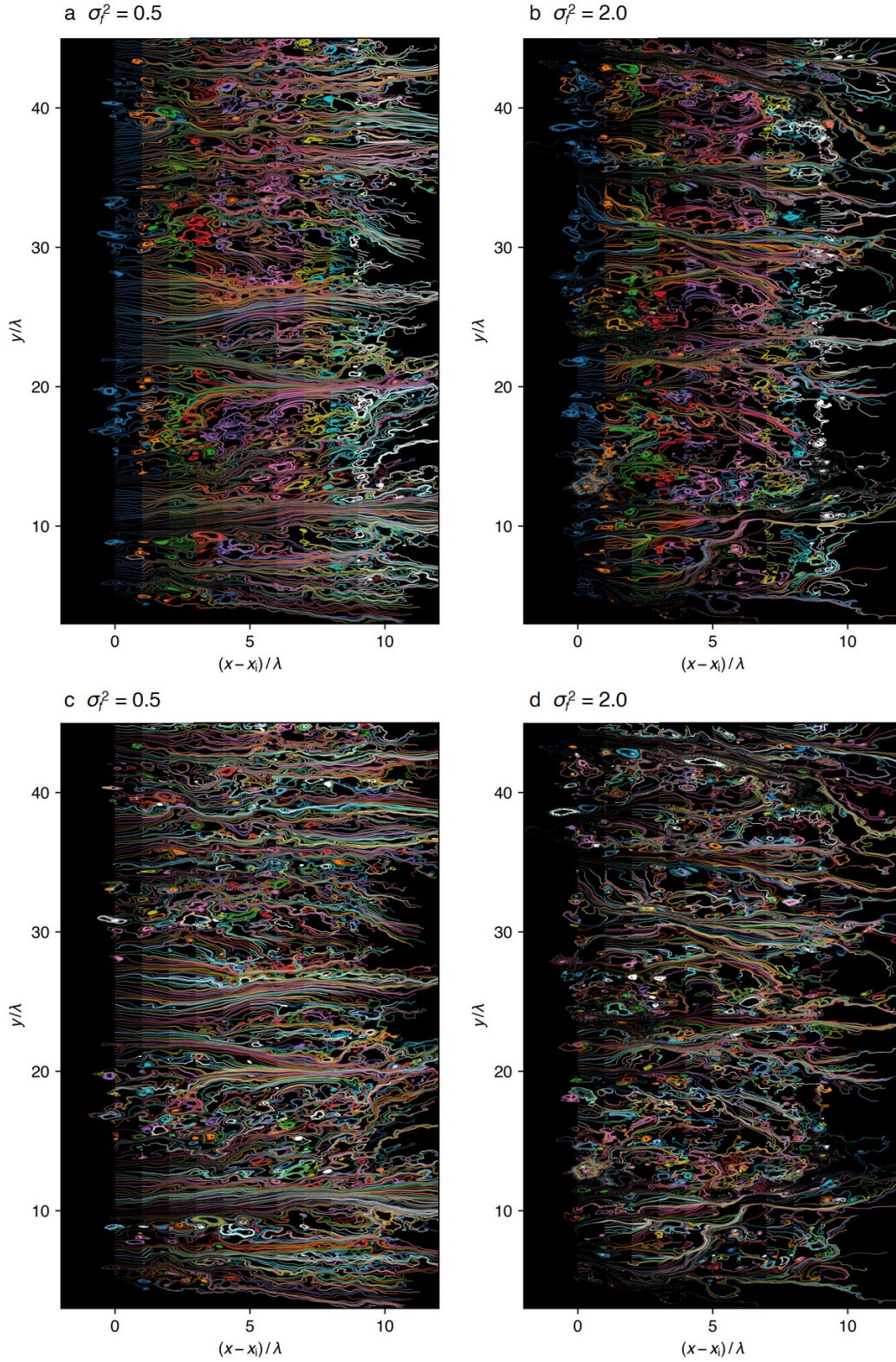


Figure 5. Poincaré sections for (a, c) $\sigma_f^2 = 0.5$ and (b, d) $\sigma_f^2 = 2.0$. All cases are purely advective ($Pe = \infty$). Particles are initially seeded at interval of $\Delta x/\lambda = 1, \Delta y/\lambda = 0.2$, and coloured dots are particle positions at $t/\tau = 1, 2, 3, \dots, 1500$. Panels with the same σ_f^2 show the same result with different colour schemes for initial particle positions along: (a, b) x - and (c, d) y -axis.

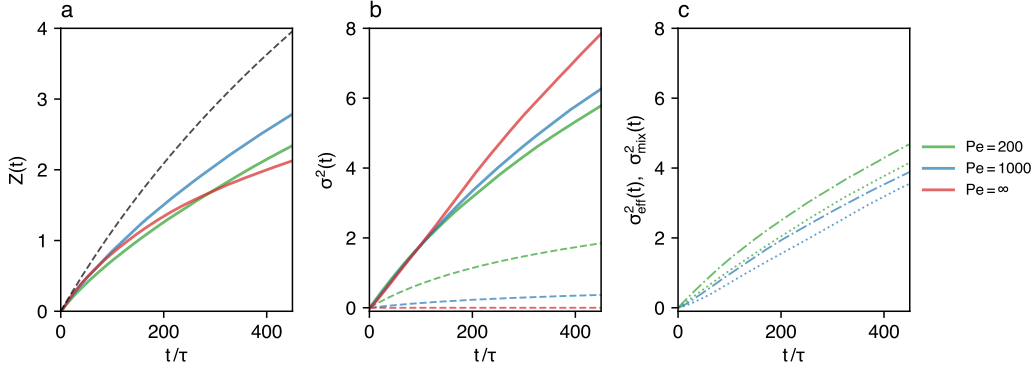


Figure 6. Temporal evolutions of period-averaged (a) centre of mass ($Z(t)$), (b) ensemble ($\sigma^2(t)$), and (c) effective (dash-dotted; $\sigma_{\text{eff}}^2(t)$) and mixing (dotted; $\sigma_{\text{mix}}^2(t)$) variances for various cases of Péclet number (Pe). Solid lines are from heterogeneous simulations ($\sigma_f^2 = 2.0$), and dashed lines in a and b are homogeneous analytical expressions.

Figure 6b shows that $\sigma^2(t)$ increases for increasing Pe . Recall that the origin of dispersion is persistent velocity contrast experienced by particles along pathlines. For small Pe , these contrasts are rapidly smoothed out by transverse dispersion compared to large Pe , similar in fact to Taylor dispersion in a tube. For equivalent homogeneous media, this is different because the variance scales with the local scale dispersivity. In fact, for infinite Pe , $\sigma^2(t) = 0$. Figure 6c shows the evolution of the effective and mixing variances for different Pe . Both are smaller than the corresponding ensemble variance, and the mixing variance is the smallest measure. Yet, both are significantly larger than the variance for an equivalent homogeneous medium. Unlike the ensemble variance, they follow a similar trend as the variance for the equivalent homogeneous media in that they decrease for increasing Pe . Recall that the ensemble variance quantifies the area swept by the solute line rather than the actual mixing area, and its magnitude is determined by the spreading of the line. The effective variance quantifies the average spreading of a point source, and the mixing variance is an actual measure for the extension of the mixing volume, which is discussed below. Thus, both measures are determined by local dispersion, especially at small times where dispersion is the only mechanism to increase the mixing area.

Figure 7 shows the dilution index, that is, the mixing area, for different heterogeneity variances and Péclet numbers. Figure 7a shows a dramatic increase in the mixing volume in the heterogeneous media compared to the equivalent homogeneous media. This increase is attributed to the significant stirring action by the heterogeneous medium illustrated in Figure 3, which manifests the increase of the line length shown in Figure 4. As for the effective and mixing variance, we observe an increase in the dilution index with decreasing Pe . Thus, a decrease of the mean displacement, which indicates containment of the plume, is concomitant with an increase of the mixing volume.

Figure 8 shows concentration point PDFs for $\sigma_f^2 = 1$ and two different Pe compared to the behaviour expected for an equivalent homogeneous medium. For homogeneous media, the PDF at small Pe is generally shifted toward smaller concentration values compared to large Pe . For the heterogeneous case, we observe the same trend because local scale dispersion is the ultimate mixing mechanism. Furthermore, at short times, the concentration PDF is expected to behave as in a homogeneous medium because mixing is primarily due to local scale dispersion, which indeed varies along the line source according to the spatially variable flow velocity. Recall that dispersion is proportional

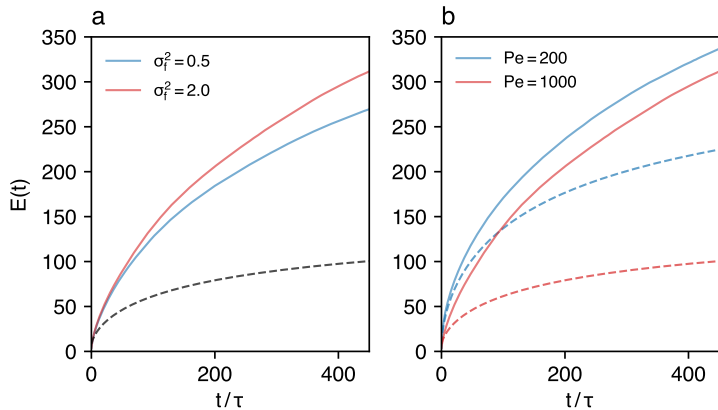


Figure 7. Temporal evolutions of period-averaged dilution index ($E(t)$) for various cases of (a) $\ln K$ variance (σ_f^2), (b) Péclet number (Pe). Unless indicated otherwise in the legend, the parameter values are $\sigma_f^2 = 2.0$ and $Pe = 1.0 \times 10^3$. Solid lines are from heterogeneous simulations, and dashed lines from homogeneous analytical expressions.

to the velocity magnitude. Thus, at short times, the PDFs for the heterogeneous and homogeneous media are qualitatively similar. At late times, however, the concentration PDFs for the heterogeneous media show a behaviour markedly different from homogeneous media. The concentration support is larger than for homogeneous media, specifically toward larger concentrations. This can be attributed to weak mixing in low-velocity zones, for which local scale dispersion is small. The probability of low concentration values on the other hand is increased compared to the homogeneous media as a consequence of increased stirring and mixing action that is also reflected in the behaviors of the effective and mixing variances and the dilution index. The concentration PDFs for low and high Péclet numbers intersect with increasing time because for low Pe the probability of high concentration values decreases faster than for high Pe and at the same time the probability for low values increases faster.

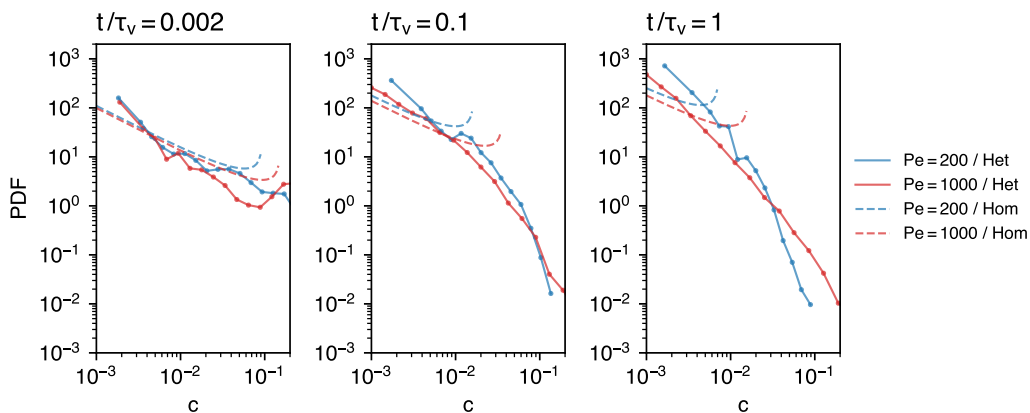


Figure 8. Temporal snapshots for probability density functions (PDFs) of concentration (c). For all cases $\kappa = 2.1$ $S_s = 1 \times 10^{-2}$. Het: numerical results for heterogeneous cases ($\sigma_f^2 = 2.0$); Hom: analytical solutions for homogeneous cases.

4 Conclusions

In conclusion, our results show that the interaction of medium heterogeneity, compressibility and temporal flow fluctuations leads to a significant increase in mixing compared to equivalent homogeneous media. While increased heterogeneity leads to relative confinement of the solute plume due to a slowing down of the growth rate of the mean displacement, it increases spreading, stirring and ultimately solute mixing. Poincaré maps of the fluctuating Lagrangian flow elucidate the origin of these behaviours, which lie in the creation of stable, regular and chaotic regions. In fact, for increasing heterogeneity, the relative proportion of these structures increases, which leads to a decrease in the advance of the mixing front and the area swept by it.

These findings have implications for a series of environmental and engineering applications that involve periodically forced flow in porous media. This includes the evaluation of the mixing of salt and freshwater in coastal aquifers under tidal forcing, as well as the assessment of groundwater remediation measures due to the periodic injection of reactants into contaminated soils or groundwater. Furthermore, our results can guide geostorage efforts that rely on the minimization of mixing with the ambient fluid, which is key in underground hydrogen storage, or its maximization, which is desired in geological carbon dioxide storage.

Appendix A Numerical implementation of particle tracking

By applying the Itô–Taylor integration scheme to the advection-dispersion equation, we write the discrete-time displacement of a particle for the case of constant porosity and isotropic dispersion as (LaBolle et al., 2000)

$$\mathbf{x}(t + \Delta t) = \mathbf{x}(t) + \mathbf{u}(\mathbf{x}, t + \Delta t) \Delta t + \mathbf{B}(\mathbf{x} + \Delta \mathbf{x}, t + \Delta t) \boldsymbol{\zeta}(t) \sqrt{\Delta t} \quad (\text{A1})$$

$$\Delta \mathbf{x} = \mathbf{B}(\mathbf{x}, t + \Delta t) \boldsymbol{\zeta}(t) \sqrt{\Delta t} \quad (\text{A2})$$

where Δt is the time step, $\mathbf{u}(\mathbf{x}, t) = \mathbf{q}(\mathbf{x}, t)/\phi$ is the Lagrangian velocity, and $\boldsymbol{\zeta}(t)$ is a Gaussian white noise with zero mean and a correlation function $\langle \zeta_i(t) \zeta_j(t') \rangle = \delta_{ij} \delta(t - t')$. For simplicity, we assume an isotropic \mathbf{D} with zero molecular diffusion ($D_m = 0$): $D_{ij} = \alpha |\mathbf{u}| \delta_{ij}$. Under this assumption, the displacement matrix \mathbf{B} is written as (Lichtner et al., 2002; Salamon et al., 2006)

$$\mathbf{B} = \begin{bmatrix} u_x \sqrt{2\alpha/|\mathbf{u}|} & -u_y \sqrt{2\alpha/|\mathbf{u}|} \\ u_y \sqrt{2\alpha/|\mathbf{u}|} & u_x \sqrt{2\alpha/|\mathbf{u}|} \end{bmatrix}. \quad (\text{A3})$$

Transport is simulated by particle tracking with our Fortran code (see Text S2 for code validation).

For calculating the particle distribution metrics for purely advective cases, $N_s = 4,000$ particles are seeded at $t = T$ along the line $x = 5\lambda (= x_i), 5\lambda \leq y \leq 45\lambda$ at a constant interval of $\Delta y = 1 \times 10^{-2}\lambda$. This number of particles is sufficiently large to ensure convergence (de Dreuzy et al., 2007). See Appendix A in Tajima et al. (2024) for details on velocity field interpolation and an adaptive time step control. We ran $N_r = 25$ simulations with different realizations of heterogeneous K fields for each case.

To calculate concentration and the related observables for cases with finite local diffusion, we performed an additional simulation ($N_r = 1$) for each case with an increased number of particles, $N_s = 100,000$, with $\Delta y = 4 \times 10^{-4}\lambda$. The concentration was calculated from the obtained particle distributions using a Gaussian kernel density estimator (Fernández-García & Sánchez-Vila, 2011).

Appendix B Effective transport in a homogeneous porous medium

For the convenience of the reader, we summarize here the results for effective transport in a homogeneous porous medium from [Pool et al. \(2016\)](#). These authors used a two-scale expansion to quantify the transport behaviour of the time-averaged concentration distribution. The time-averaged concentration $\bar{c}_0(x, t)$ satisfies the advection-dispersion equation

$$\frac{\partial \bar{c}_0(x, t)}{\partial t} + \frac{\partial}{\partial x} v_e(x) \bar{c}_0(x, t) - \frac{\partial^2}{\partial x^2} [D_e(x) + D_0] \bar{c}_0(x, t) = 0, \quad (\text{B1})$$

which describes solute transport for $t \gg \tau$. The effective transport velocity and dispersion coefficient are given by

$$v_e(x) = \frac{v_0^2 \mu \tau \exp(-\mu x)}{4\pi}, \quad D_e(x) = \frac{2\alpha v_0}{\pi} \exp(-\mu x). \quad (\text{B2})$$

Based on this effective formulation, [Pool et al. \(2016\)](#) derive the following approximate solutions for the centre of mass position and displacement variance,

$$Z(t) = \frac{1}{2\mu} \ln \left(\frac{t}{\tau_v} + 1 \right) \quad (\text{B3})$$

$$\sigma_e^2(t) = \frac{\sigma_0^2}{(1 + t/\tau_v)^2} + \frac{4D_e\tau_v}{5} \left[\frac{(1 + t/\tau_v)^{\frac{5}{2}} - 1}{(1 + t/\tau_v)^2} \right] + 2D_0t \left[\frac{1}{3} + \frac{(t/\tau_v)^2 - 1}{3t/\tau_v(1 + t/\tau_v)^2} \right], \quad (\text{B4})$$

where $\sigma_0^2 = \sigma^2(t = 0)$ is the initial variance. In this study, we set $\sigma_0^2 = 0$ and $D_0 = 0$. These authors find that the concentration distribution can be approximated by the one-dimensional Gaussian distribution

$$c(\mathbf{x}, t) = \frac{1}{\ell_0} \frac{\exp \left(-\frac{[x - z_0(t)]^2}{2\sigma^2(t)} \right)}{\sqrt{2\pi\sigma^2(t)}}, \quad (\text{B5})$$

where $\sigma_e^2(t)$ is given by Equation (B4).

For the Gaussian concentration distribution (Equation B5), the dilution index can be determined explicitly and is given by

$$E(t) = \ell_0 \sqrt{2e\pi\sigma^2(t)}. \quad (\text{B6})$$

Similarly, one obtains for the concentration PDF the explicit analytical expression

$$\Pi(c, t) = \frac{\mathbb{I}[c_{\text{th}} < c \leq c_{\text{max}}(t)]}{2c\sqrt{\ln[c_{\text{max}}(t)/p] \ln[c_{\text{max}}(t)/c_{\text{th}}]}}, \quad (\text{B7})$$

where $\mathbb{I}(\cdot)$ is the indicator function, which is one if its argument is true and zero otherwise, c_{th} is the threshold concentration value, and $c_{\text{max}}(t)$ is the maximum concentration in the domain at each time, given from Equation (B5) by

$$c_{\text{max}}(t) = \frac{1}{\ell_0 \sqrt{2\pi\sigma^2(t)}}. \quad (\text{B8})$$

Appendix C Concentration PDFs with pure diffusion

Figure 8 illustrates that the largest concentration value in the heterogeneous cases becomes higher than that in the homogeneous cases. We hypothesize that this result is attributed to the particle entrapment by low-velocity regions in heterogeneous media. To confirm this hypothesis, we consider additional cases with finite diffusion, which is constant and independent of velocity, instead of the velocity-dependent local dispersion assumed throughout this study. The dispersion tensor \mathbf{D} here becomes

$$D_{ij} = D_0 \delta_{ij} \quad (\text{C1})$$

where $D_0 = \alpha v_0$.

Figure C1 shows that the maximum concentration value in the heterogeneous case is smaller than the homogeneous case, which is opposite from the cases with velocity-dependent local dispersion (Figure 6 in the main article). This observation suggests that particles can escape from the low-velocity regions in heterogeneous media with diffusion independent of velocity, corroborating the hypothesis above. Meanwhile, as observed in the dispersive cases, Figure C1 illustrates that dilution is enhanced in the heterogeneous case compared to the homogeneous case.

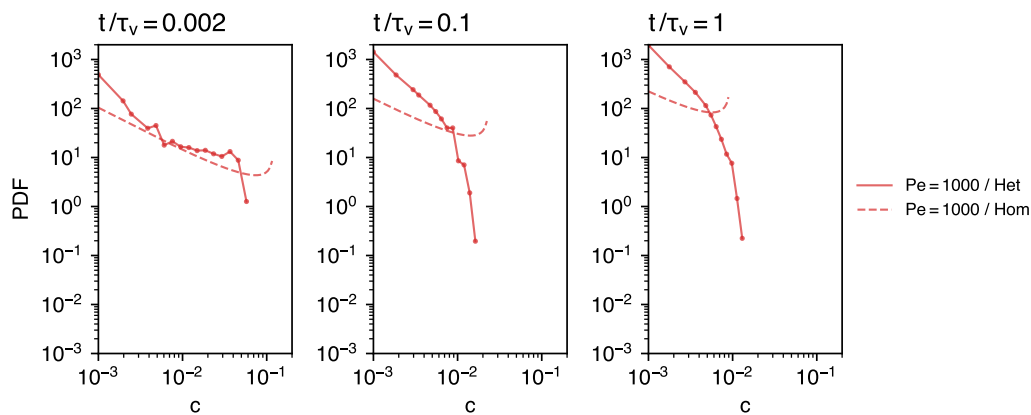


Figure C1. Temporal snapshots for probability density functions (PDFs) of concentration (c) with pure diffusion. For all cases $Pe = 1000$. Het: numerical results for heterogeneous cases ($\sigma_f^2 = 2.0$); Hom: analytical solutions for homogeneous cases.

Acknowledgments

S. Tajima acknowledges the financial support by the JSPS KAKENHI Grant Number JP23KJ0431 (Grant-in-Aid for JSPS Fellows). The Authors thank Daniel Lester (RMIT University) for insightful discussions.

References

- Ataie-Ashtiani, B., Volker, R., & Lockington, D. (1999). Tidal effects on sea water intrusion in unconfined aquifers. *Journal of Hydrology*, 216(1-2), 17–31.
- Bailey, R. T., & Jenson, J. W. (2014). Effects of marine overwash for atoll aquifers: environmental and human factors. *Groundwater*, 52(5), 694–704.

- Bear, J. (1988). *Dynamics of fluids in porous media*. Dover.
- Cirpka, O. A., & Attinger, S. (2003). Effective dispersion in heterogeneous media under random transient flow conditions. *Water Resources Research*, *39*(9).
- Dagan, G. (1982). Stochastic modeling of groundwater flow by unconditional and conditional probabilities: 2. the solute transport. *Water Resources Research*, *18*(4), 835–848.
- Dagan, G. (2012). *Flow and transport in porous formations*. Springer Science & Business Media.
- Dagan, G., Bellin, A., & Rubin, Y. (1996). Lagrangian analysis of transport in heterogeneous formations under transient flow conditions. *Water Resources Research*, *32*(4), 891–899.
- de Dreuzy, J.-R., Beaudoin, A., & Erhel, J. (2007). Asymptotic dispersion in 2d heterogeneous porous media determined by parallel numerical simulations. *Water Resources Research*, *43*(10).
- de Dreuzy, J.-R., Carrera, J., Dentz, M., & Le Borgne, T. (2012). Asymptotic dispersion for two-dimensional highly heterogeneous permeability fields under temporally fluctuating flow. *Water Resources Research*, *48*(1).
- Dentz, M., & Carrera, J. (2003). Effective dispersion in temporally fluctuating flow through a heterogeneous medium. *Physical Review E*, *68*(3), 036310.
- Dentz, M., Hidalgo, J. J., & Lester, D. (2023). Mixing in porous media: concepts and approaches across scales. *Transport in Porous Media*, *146*(1-2), 5–53.
- Fernández-García, D., & Sánchez-Vila, X. (2011). Optimal reconstruction of concentrations, gradients and reaction rates from particle distributions. *Journal of contaminant hydrology*, *120*, 99–114.
- Ferris, J. G. (1952). *Cyclic fluctuations of water level as a basis for determining aquifer transmissibility* (Tech. Rep.). US Geological Survey.
- Gelhar, L. W., & Axness, C. L. (1983). Three-dimensional stochastic analysis of macrodispersion in aquifers. *Water Resources Research*, *19*(1), 161–180.
- Inouchi, K., Kishi, Y., & Kakinuma, T. (1990). The motion of coastal groundwater in response to the tide. *Journal of Hydrology*, *115*(1), 165-191. doi: [https://doi.org/10.1016/0022-1694\(90\)90203-A](https://doi.org/10.1016/0022-1694(90)90203-A)
- Jacob, C. (1950). Flow of groundwater. *Engineering hydraulics*, 321–386.
- Jiao, J. J., & Tang, Z. (1999). An analytical solution of groundwater response to tidal fluctuation in a leaky confined aquifer. *Water Resources Research*, *35*(3), 747–751.
- Kinzelbach, W. (1988). The random-walk method in pollutant transport simulation. *NATO ASI Ser., C*(224), 227–246.
- Kinzelbach, W., & Ackerer, P. (1986). Modelisation de la propagation d'un contaminant dans un champ d'écoulement transitoire. *Hydrogeologie*, *2*, 197–205.
- Kitanidis, P. K. (1988). Prediction by the method of moments of transport in a heterogeneous formation. *Journal of Hydrology*, *102*(1-4), 453–473.
- Kitanidis, P. K. (1994). The concept of the dilution index. *Water resources research*, *30*(7), 2011–2026.
- LaBolle, E. M., Quastel, J., Fogg, G. E., & Gravner, J. (2000). Diffusion processes in composite porous media and their numerical integration by random walks: Generalized stochastic differential equations with discontinuous coefficients. *Water Resources Research*, *36*(3), 651–662.
- Langevin, C. D., Hughes, J. D., Banta, E. R., Niswonger, R. G., Panday, S., & Provost, A. M. (2017). *Documentation for the modflow 6 framework: U.s. geological survey techniques and methods* (Tech. Rep.). US Geological Survey.
- Li, H., & Jiao, J. J. (2002). Analytical solutions of tidal groundwater flow in coastal two-aquifer system. *Advances in Water Resources*, *25*(4), 417–426.
- Li, L., Barry, D., Stagnitti, F., & Parlange, J.-Y. (2000). Groundwater waves in a coastal aquifer: A new governing equation including vertical effects and capillarity. *Water Resources Research*, *36*(2), 411–420.

- Lichtner, P. C., Kelkar, S., & Robinson, B. (2002). New form of dispersion tensor for axisymmetric porous media with implementation in particle tracking. *Water Resources Research*, 38(8), 21-1-21-16. doi: <https://doi.org/10.1029/2000WR000100>
- Nielsen, P. (1990). Tidal dynamics of the water table in beaches. *Water resources research*, 26(9), 2127–2134.
- Oberdorfer, J. A., Hogan, P. J., & Buddemeier, R. W. (1990). Atoll island hydrogeology: flow and freshwater occurrence in a tidally dominated system. *Journal of Hydrology*, 120(1-4), 327–340.
- Pool, M., & Dentz, M. (2018). Effects of heterogeneity, connectivity, and density variations on mixing and chemical reactions under temporally fluctuating flow conditions and the formation of reaction patterns. *Water Resources Research*, 54(1), 186–204.
- Pool, M., Dentz, M., & Post, V. E. A. (2016). Transient forcing effects on mixing of two fluids for a stable stratification. *Water Resources Research*, 52(9), 7178–7197. doi: 10.1002/2016WR019181
- Pool, M., Post, V. E., & Simmons, C. T. (2014). Effects of tidal fluctuations on mixing and spreading in coastal aquifers: Homogeneous case. *Water Resources Research*, 50(8), 6910–6926.
- Pool, M., Post, V. E., & Simmons, C. T. (2015). Effects of tidal fluctuations and spatial heterogeneity on mixing and spreading in spatially heterogeneous coastal aquifers. *Water Resources Research*, 51(3), 1570–1585.
- Rehfeldt, K. R., & Gelhar, L. W. (1992). Stochastic analysis of dispersion in unsteady flow in heterogeneous aquifers. *Water Resources Research*, 28(8), 2085–2099.
- Renard, P., & de Marsily, G. (1997). Calculating equivalent permeability: a review. *Adv. Water Res.*, 20, 253–278.
- Risken, H. (1996). *The fokker-planck equation*. Springer Heidelberg New York.
- Salamon, P., Fernández-García, D., & Gómez-Hernández, J. (2006). Modeling mass transfer processes using random walk particle tracking. *Water Resources Research*, 42(11).
- Tajima, S., Brunner, P., Liu, J., Delottier, H., & Tokunaga, T. (2023). Groundwater flooding on atolls caused by storm surges: Effects of the dual-aquifer configuration. *Water Resources Research*, 59(10), e2023WR034762. doi: 10.1029/2023WR034762
- Tajima, S., Dentz, M., Liu, J., & Tokunaga, T. (2024). Time-dependent dispersion coefficients for the evolution of displacement fronts in heterogeneous porous media. *Advances in Water Resources*, 104714. doi: 10.1016/j.advwatres.2024.104714
- Terry, J. P., & Falkland, A. C. (2010). Responses of atoll freshwater lenses to storm-surge overwash in the northern cook islands. *Hydrogeology journal*, 18(3), 749.
- Wu, J., Lester, D., Trefry, M. G., & Metcalfe, G. (2024). Lagrangian coherent structures control solute dispersion in heterogeneous poroelastic media. *Phys. Rev. Fluids*, 9(044501).
- Zivar, D., Kumar, S., & Foroozesh, J. (2021). Underground hydrogen storage: A comprehensive review. *Int. J. Hydrogen Energy*, 46, 23436–23462.